# Experimental study on the effect of adaptive flaps on the aerodynamics of an Ahmed body

J. M. Camacho-Sánchez [ORCID],[1] M. Lorite-Díez [ORCID],[2,3,*] J. I. Jiménez-González [ORCID],[1]
O. Cadot [ORCID],[4] and C. Martínez-Bazán [ORCID][2,3]

[1]*Departamento de Ingeniería Mecánica y Minera, Universidad de Jaén, 23071 Jaén, Spain*
[2]*Departamento de Mecánica de Estructuras e Ingeniería Hidráulica, Universidad de Granada, 18001 Granada, Spain*
[3]*Andalusian Institute for Earth System Research, University of Granada, 18006 Granada, Spain*
[4]*Department of Aerospace Engineering, University of Liverpool, L69 3GH Liverpool, United Kingdom*

We perform an experimental study on the turbulent flow around a square-back Ahmed body of height, $h$, at varying $Re = u_\infty h/\nu \in [0.5, 1] \times 10^5$, where $u_\infty$ is the free-stream velocity and $\nu$ is the incoming flow kinematic viscosity, under different yaw angles $\beta = (0°, -5°, -10°)$, to analyze the use of rear flexibly hinged parallel plates as a control strategy to reduce the drag in a self-adaptive manner under changing flow conditions. The model implements rear parallel rigid flaps of depth $d = 0.5h$, which are mounted with torsional joints through embedded flexible foils of calibrated thickness. This holding system restricts the motion of the plates to a rotary displacement, $\theta$. The fluid-structure dynamics is characterized by the reduced velocity, defined as $U^* = u_\infty/f_n h$, where $f_n$ is the natural frequency of rotary oscillations of the hinged plates, measured in free-decay tests of flaps. In fact, we have explored the range of reduced velocity, $U^* = [0, 65]$, varying $u_\infty$ and consequently Re. We perform force and pressure measurements to quantify the variations of the drag and the base pressure coefficients while laser displacement sensors are used to obtain the angular flaps motion. Results show that the hinged plates decrease the drag coefficient of the original body by nearly 4.4% for flow conditions aligned with the body axis. Under cross-flow conditions, their efficiency is even larger, attaining relative reductions drag of nearly 9.1% at $\beta = -10°$ (13.5% in comparison with a body with fixed rigid plates of the same depth). Such variations are shown to be associated with a passive reconfiguration process of rear flaps. Additionally, hinged flaps are shown to interact with the reflectional-symmetry-breaking (RSB) modes, typically present in the wake of three-dimensional bodies. At aligned conditions, the interaction with the RSB modes is characterized by two regimes, in such a way that the hinged flaps manage to partially stabilize the RSB modes, and consequently to inhibit the bistable behavior at low values of $U^*$ (in a similar manner to rigid flaps), while at high values of $U^*$, they respond dynamically to switches between the opposite wake deflections of the RSB modes, deviating themselves accordingly.

## I. INTRODUCTION

Recent international context has raised significant environmental and economic concerns related to energy consumption and associated greenhouse emission gases. Heavy road transport industry

---

*mldiez@ugr.es

044605-1

represents a major source of $CO_2$ emissions, due to their associated aerodynamically inefficient blunt geometry, which favors energy consumption. Hence, fundamental research on drag reduction, aiming to enhance fuel efficiency, may help developing effective strategies to render transport more sustainable and achieve environmental goals in the short term.

The drag experienced by a vehicle in motion is mainly constituted of pressure drag and friction drag. For a blunt-based simplified vehicle, e.g., truck, the pressure drag may represent up to 85% of the total drag [1]. Ahmed *et al.* [1] also found that the rear end contributes as much as 91% to the total pressure drag and is especially predominant at high speeds, as reported by Hucho and Sovran [2]. Furthermore, it is estimated that approximately 25% of the air resistance of a heavy vehicle in real conditions is connected to its rear end [3]. Consequently, most of the flow control strategies developed over the past years, have been mainly designed to act on the flow separation at the rear end of the vehicle and the near-wake region [4].

The complex geometries of road vehicles are usually simplified for research and academic studies, while preserving the main features of the flow and aerodynamics characterizing real vehicles. For instance, the model proposed by Ahmed *et al.* [1] has been broadly studied in their two versions: with a slanted trailing edge or with a square-back geometry. In the present study, we focus on the square-back Ahmed body, whose aerodynamics has been extensively described in Refs. [5–9]. This model features a large drag on account of the massive flow separation at the rear edges, that creates a large recirculating region associated with low pressure. Besides, the presence of reflectional-symmetry-breaking (RSB) modes sets the asymmetry and dynamics of the near wake [7]. Under typical wind tunnel conditions, RSB modes dynamics is characterized by the stochastic switching between two horizontal symmetrically deflected positions of the wake for the Ahmed body. These modes induce additional side force on the body and an increase in drag [8], as they impact the base pressure distribution, so that the control strategies may be designed to retrieve wake symmetry by partially stabilizing the RSB modes.

Among other different strategies, applying a rear cavity to the base of the geometry by extending plates from the base of the geometry, is one way to reduce the drag [4] and manipulate the afore-mentioned RSB modes. When applied perpendicular to the base, they are effective on simplified geometries at aligned flow conditions [10], yielding up to an 9% drag reduction due to the increase of the base pressure.

However, road vehicles often operate under cross-flow conditions. Therefore, it is necessary to evaluate forces and flow features of simplified heavy vehicle models over wide ranges of the yaw angle, $\beta$, which accounts for the misalignment of the model with respect to the incident free stream. The presence of side wind can significantly alter the flow detachment and the near-wake properties, thus leading to the increase of side and drag forces, and the vehicle's instability [2]. In particular, typical studies of crosswind are focused on the range given by $\beta \in [-10°, 10°]$, which are representative limits of the yaw angle for typical driving conditions [2,11], and are in line with the new requirements for vehicles testing in the European Union.

In this regard, Howell *et al.* [12] highlighted the importance of these studies by presenting several real vehicles with a very similar drag coefficient at $\beta = 0°$ yaw, that had a very different drag response to crosswind. Also, Fan *et al.* [13] analyzed the effect of yawed conditions on the pressure distribution and RSB modes on the square-back Ahmed body, indicating a strong effect on the horizontal and vertical base pressure gradients.

In terms of control strategies, Lorite-Díez *et al.* [14] showed that the performance of a straight cavity as drag reducer is dramatically decreased under cross-flow conditions. There, they proposed the use of a curved cavity (whose profile was obtained by means of previous shape optimization in two-dimensional (2D) flows [15]), that improves the effect of a straight cavity under aligned and yawed conditions. Other authors have also analyzed the performance of different symmetric control and drag reduction devices under cross flow, such as boat tailing [16], tapered cavities [21], or pulsed jets actuators [17], showing a good capacity to reduce the drag.

Additionally, some recent studies have investigated the influence of asymmetric drag reduction devices with side-wind conditions using tapering or lateral flaps [18–20]. In particular, as reported

by García de la Cruz *et al.* [19], symmetric configurations of flaps do not provide optimal drag reductions under yawed conditions. On the contrary, largest reductions are obtained for different angle of deflection. Similar observations were made by Urquhart *et al.* [22], who used surrogate model-based algorithm to define optimal flaps orientations under aligned and yawed conditions for a blunt-base vehicle model. They showed that optimizing the angle of each flap individually, under cross-flow conditions, can lower drag by enforcing the near-wake symmetry through weakening of the large leeward side vortex. This type of surrogate model-based optimization techniques have been successfully employed by the same group to more realistic vehicles [23], to reduce drag at different yaw angles, by continually optimizing and modifying positions of servo-controlled flaps at a given wind speed.

In spite of the previous works on the optimization of passive systems to reduce drag and control the wake under changing flow conditions, to the best of the authors' knowledge, the effect of self-adaptive systems undergoing a passive reconfiguration with the flow on the aerodynamics and wake dynamics behind an Ahmed body has not been studied before. Thus, following this idea, and inspired in biological applications of reconfiguration processes involving flexible or movable parts [24–26], we propose to analyze the performance of flexibly hinged flaps that adapt to flow conditions dynamically. Previous experimental and numerical analyses of two-dimensional or extruded blunt bodies implementing flexible plates at the rear edges [27–30], show the ability of flaps to render the trailing edge more aerodynamic, and therefore, decrease the drag. This is an appealing approach, which remains unexplored in three-dimensional blunt-based models, such as the Ahmed body, whose unsteady wake dynamics is considerably more complex than that of two-dimensional bodies. Therefore, the aim of the paper consists in the exploration of self-adaptive systems of flaps, which allows dynamic reorientation under changing flow conditions and regimes, on the aerodynamics and wake dynamics of the square-back Ahmed body.

The paper is organized as follows. The problem description and experimental details are introduced in Sec. II. Next, Sec. III is devoted to analyze the results, comparing force, pressure and hinged-plates angular displacement measurements obtained under the different configurations. In particular, we first describe in Sec. III A the drag evolution and its modification mechanism for the tested configurations at aligned and crosswind conditions. Then, lateral aerodynamic loads, particularly important in this problem, are discussed in Sec. III B. The role of the lateral flaps and specially, the effect of hinged flaps in terms of RSB modes interaction, and the potential mechanisms involved, is presented in Sec. III C. Finally, the main conclusions are drawn in Sec. IV.

## II. PROBLEM DESCRIPTION AND EXPERIMENTAL DETAILS

### A. Experimental description

We study experimentally the turbulent wake behind a square-back Ahmed body of length $l = 261$ mm, width $w = 97.25$ mm, and height $h = 72$ mm as in Ref. [31]. The model is placed inside a recirculating wind tunnel (see Fig. 1), available at the University of Jaén, with a nozzle of 8:1 contraction ratio connected to a $400 \times 400$ mm$^2$ test section, where turbulent intensity of the flow is around 1%. In the present work, the Reynolds number varies in the range Re $= \rho u_\infty h/\mu \in$ [48000, 96000], where $u_\infty$ denotes the free-stream velocity, $\rho$ and $\mu$ the fluid density and dynamic viscosity, respectively. The coordinate system is included in Fig. 1, whose origin is set at the center of the Ahmed body base, $x$ being the direction perpendicular to the body base, $z$ the vertical direction from the wind tunnel floor, and $y$ the direction that forms a right-hand trihedron. In addition, rotation angles $(\beta, \theta_1, \theta_2)$ in the $(x, y)$ plane are defined positive in the counterclockwise sense as indicated on the coordinate system shown in Fig. 1. The yaw angle, $\beta$, is set, by means of an automated turntable that allows a precise rotational placement of the model with an accuracy of 0.01 ° (see Fig. 1), to account for crosswind conditions. Three different yaw angles $\beta = [0°, -5°, -10°]$ are studied as typical crosswinds of on-road conditions [12]. Note that, for the considered Reynolds number range and the maximum yaw of $-10°$, the rear separation still remains fixed at the trailing
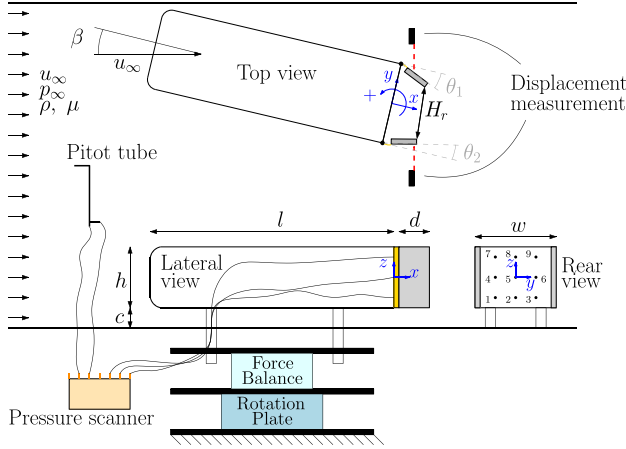
FIG. 1. Sketch of the experimental setup.

edge of the rectangular base as shown by previous wake velocity measurements [14]. It indicates that the separation at the body nose always reattaches before the trailing edge and a situation of a rear wake separated from the nose that would appear at lower Re is never met. Hence, although the Reynolds number considered in this paper is one or two orders of magnitude lower than that of real vehicles with blunt trailing edges, the flow at the base may share the same properties of rear separation. The ground clearance is precisely set to $c/h = 0.278$ ($c = 20$ mm). The model associated blockage is 4% at aligned conditions and 6.5% at $\beta = -10°$.

Here, we study the influence of two flexibly hinged rigid plates of depth $d = 0.5\,h$ that are mounted at the lateral rear edges of the model. The flaps deflections are $\theta_1$ and $\theta_2$ (see Fig. 1) corresponding, respectively, to the leeward and windward flap under the tested cross-flow conditions ($\beta = -5°, -10°$). Each flexible hinged flap is composed of a thin metallic foil (steal) of calibrated thickness $e_f/h = 3.5 \times 10^{-4}$ and a rigid plate of thickness $e_s/h = 6.9 \times 10^{-3}$ and density $\rho_s$ [Fig. 2(a)]. When mounted together at the base of the model, using a 3D printed part, the system behaves as an angular oscillator of one degree of freedom, with effective torsional stiffness $k$, damping $\zeta$ and mass moment of inertia $J$.

An illustration of a typical free-decay test is shown in Fig. 2(b), where the instantaneous angular displacement with respect to the center of rotation $\theta(t)$ is depicted, along with its corresponding instantaneous fluctuating amplitude $\hat{\theta}(t)$ or envelope (which can be computed, e.g., by applying the Hilbert transform). The natural frequency $f_n$ of the system is easily obtained from the oscillation cycles, whereas the damping ratio $\xi$ is determined from the envelope's exponential function $e^{-2\pi f_n \xi}$ (note that the structural damping may be obtained as $\zeta = 4\xi\pi f_n J$). The free-decay test parameters are obtained after performing six independent runs with an uncertainty below $\pm 0.1$ Hz for $f_n$ and $\pm 0.0007$ for the damping ratio.

The fluid-structure interaction problem is then defined by means of the nondimensional mass ratio of the system, $m^* = \rho_s/\rho_f \simeq 6250$, the combined mass-damping parameter $\xi m^* \simeq 80$, and the reduced velocity,

$$U^* = \frac{u_\infty}{f_n h},\tag{1}$$

which quantifies the dimensionless stiffness.

In that view, the dimensionless stiffness of the hinged system can be easily changed by varying the free-stream velocity without modifying the experimental foil-flap arrangement. By doing so, the Reynolds number Re does not remain constant, however, the aerodynamic effect provided by the variation of the velocity $u_\infty$ can be analyzed by studying initially the features of the reference
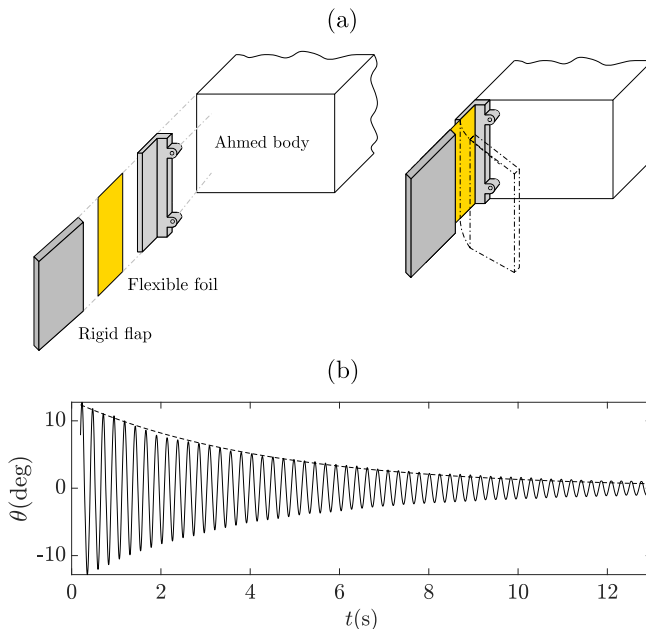
FIG. 2. (a) Detail of the flexibly-hinged flap system. (b) Instantaneous angular displacement $\theta(°)$ of the flap from a free-decay test.

model without hinged flaps. In this work, we present results from three different configurations, named: case B, baseline Ahmed body without any rear device; case RF, Ahmed body implementing static rigid flaps of depth $d = 0.5h$, i.e., $U^* \rightarrow 0$; and finally, case HF, Ahmed body implementing flexible hinged flaps of $d = 0.5h$ depicted in Fig. 2(a).

### B. Forces, base pressure, and plates displacement measurements

Force, pressure, and flaps displacement measurements were acquired during experiments under controlled conditions. Several runs were defined for each test case in order to ensure repeatability of results.

The aerodynamic forces along the local coordinate axes, i.e., drag force $f_x$ and side force $f_y$ were measured using a precise six-axis load cell, connected to the model through four cylindrical supports of diameter 7.5 mm (Fig. 1), so the balance is rotated with the body, fixing the coordinate system in the Ahmed base. The force coefficients are then obtained as,

$$c_i = \frac{2\,f_i}{\rho u_\infty^2 hw}, \tag{2}$$

where $c_x$ and $c_y$ are the drag and lateral force coefficients. The force measurements have an associated uncertainty below $\pm\,0.001$ for $c_{x,y}$.

As illustrated in Fig. 1, the base pressure was measured with help of taps distributed in a $3 \times 3$ equispaced grid with $\Delta y = 0.26h$ mm and $\Delta z = 0.18h$ mm, providing with local pressure values $p_i(i = 1, 2, \ldots, 9)$. The acquisition was performed by means of a 64-channel pressure scanner with a sampling frequency of 200 Hz providing an accuracy of 0.6 Pa per channel. Base pressure measurements will be expressed in terms of the pressure coefficient as

$$c_{p,i} = \frac{p_i - p_\infty}{\rho u_\infty^2/2}, \tag{3}$$

where $p_\infty$ is the free-stream pressure, registered using a Pitot tube placed upstream of the model. The uncertainty associated with $c_{p,i}$ values is below $\pm 0.001$ in the present experiments. In addition, the base drag coefficient [32] will be estimated by means of

$$c_B = -\frac{1}{n}\sum_{i=1}^{n} c_{p,i} \tag{4}$$

being $n = 9$ the total number of base pressure taps. Besides, following previous studies (see, e.g., Refs. [7,14]) the wake asymmetry can be quantified with help of the horizontal and vertical pressure gradients, i.e., $g_y$ and $g_z$, calculated as

$$g_y = h\frac{\partial c_p}{\partial y} \simeq \frac{1}{2}h\left[\frac{c_{p,6} - c_{p,4}}{y_6 - y_4}\right], \tag{5}$$

$$g_z = h\frac{\partial c_p}{\partial z} \simeq \frac{1}{2}h\left[\frac{c_{p,8} - c_{p,2}}{z_8 - z_2}\right]. \tag{6}$$

Note that this nine-pressure-tap arrangement can be used a as representative set-up to estimate accurately base drag and base pressure gradients. The reason is that the wall pressure distribution in the separated area is at first order almost constant in one direction and affine in the other perpendicular direction (direction of the asymmetry) (see, e.g., Ref. [33]).

Finally, the displacement of the rear flaps was recorded by means of optical laser sensors (see Fig. 1). These sensors measured the linear displacement of the flaps' tips, from which, after application of adequate trigonometric transformation, the instantaneous angular deflections $\theta_1$ and $\theta_2$ were obtained. The linear resolution provided by the laser sensor translates into an angular accuracy of 0.0005 rad. As depicted in Fig. 1, these angles are zero for a flap aligned with the body lateral side and defined positive in the counterclockwise sense.

In the following, time-dependent variables will be denoted using lowercase letters $a$, while time-averaged values will be expressed by means of uppercase letters $A = \bar{a}$. In addition, $\hat{a}$ will denote instantaneous fluctuating amplitude of the variable $a$, which will be computed by means of the Hilbert transform, so that $\hat{A}$ will represent the corresponding time-averaged fluctuating amplitude.

### C. Drag decomposition

Since the drag is defined as the aerodynamic force component along the body axis, all pressure forces on lateral surfaces (i.e. having wall normal directions perpendicular to this axis) do not contribute to the drag, whatever the yaw is. This is the case for the four sides of the baseline body and for the rigid plates from RF configuration. However, these surfaces still contribute to the drag through friction. Our drag, $C_x$, and base drag, $C_B$, measurements allow the following drag decomposition,

$$C_x = C_B + C_R, \tag{7}$$

where $C_R$ is a coefficient that comprises all the drag contributions except the body base one such as the body supports, the frictional drag on the four lateral body sides and the body nose. It also accounts for the flaps when they are added. Therefore, it is possible to assess the drag contribution of the flaps assuming that between the body with flaps (RF or HF configurations) and the baseline (B configuration), the drag contributions due to the nose, the supports, and the four lateral sides are the same at a given yaw. That assumption can be reasonable since the only body surfaces that could be sensitive to the flaps' presence are the rear part of the four lateral sides. As they only contribute through friction, they are known to be a small contributor to drag [1] at the tested Re. Under this assumption, $\Delta C_R = \Delta C_x - \Delta C_B$ can be seen as the direct drag contribution of the aerodynamic force exerted on the flaps, where the difference $\Delta$ is operated from the baseline B, e.g., $\Delta C_{R,\mathrm{HF}} = C_{R,\mathrm{HF}} - C_{R,\mathrm{B}}$.
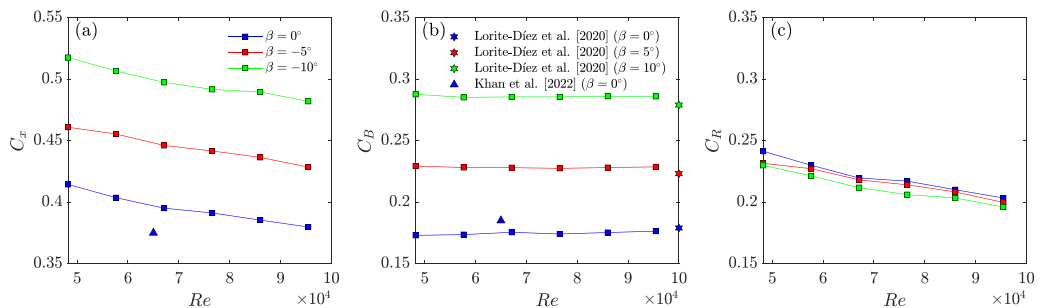
FIG. 3. Evolution of the (a) averaged drag $C_x$, (b) base drag $C_B$, and (c) remaining drag $C_R$ coefficients with the Reynolds number for the baseline case (B, squares) at different yaw angles ($\beta = 0°$ in blue, $\beta = -5°$ in red and $\beta = -10°$ in green).

## III. RESULTS

### A. Drag reduction

We first present results from time-averaged drag $C_x$, base drag $C_B$, and $C_R$ coefficients and their evolution with the Reynolds number for the baseline Ahmed body (denoted case B) at different tested yaw angles $\beta$ in Fig. 3. Regardless of the value of $\beta$, $C_x$ is reduced when $Re$ increases, as the friction drag is reduced [see Fig. 3(a)]. In fact, Fig. 3(b) shows that the pressure drag, estimated here by means of $C_B$, does not depend on Re for any yaw orientation. The remaining body drag, expressed by $C_R$, is reduced when Re increases as it compromises the friction drag.

Besides, both drag and base drag coefficients increase as the yaw angle of the body with respect to the streamwise direction grows. Lorite-Díez *et al.* [14] reported a linear variation between $C_x$ (or $C_B$) with $\beta$, indicating that the drag coefficient increases with the yaw angle due to a decrease in the base pressure associated with a shorter recirculation region. Such variation might be also related to the flow separation observed along the longitudinal edges of the Ahmed body [34]. Although these streamwise vortices are not investigated herein, their contribution to the drag at yaw are naturally integrated in the measured base suction and force coefficients.

The same linear variation between drag and yaw angle can be inferred from Fig. 3. Also, note that the values of $C_x$ and $C_B$ obtained in the present work are in good agreement with results previously reported for similar setups [14,35]. Interestingly, $C_R$ decreases with yaw, which might be due to the thrust produced by the pressure loading around the body nose at yaw reported by Ref. [13] for the Ahmed body.

The values of the time-averaged drag coefficients featured by the baseline model will be used as reference in Fig. 4 to illustrate the effect of the rigid (RF case) and hinged flaps (HF case) on the body drag for the Reynolds numbers tested, and the corresponding range of reduced velocity $U^*$ for the flexible flaps arrangement. The reference values and the respective relative reductions of drag, base drag, and remaining drag coefficient are listed in Table I.

That said, under aligned flow conditions, $\beta = 0°$, the RF configuration reduces efficiently the base drag $C_B$ by approximately $\Delta C_B \simeq -12\%$ for all the tested values of Re. However, drag reductions are small, being the largest variation $\Delta C_x \simeq -1.9\%$. This may stem from the fact that, when the flaps are mounted, the body surface increases and so does the friction drag, and consequently, $C_R$, which offsets the reduction given by $C_B$. These results are consistent with previously reported data for a closed rigid cavity in Ref. [14], where the achieved reduction for base drag coefficient ($\Delta C_B = -0.043$) is almost twice that of the drag coefficient ($\Delta C_x = -0.022$). It seems reasonable to think that the reductions attained herein are smaller on account of the flow separation along top and bottom edges of the base, where no flaps are installed.

On the other hand, the use of hinged flaps (HF configuration) reduces more efficiently the base drag $C_B$, although, again, the drag improvement is smaller, likely due to a larger friction drag
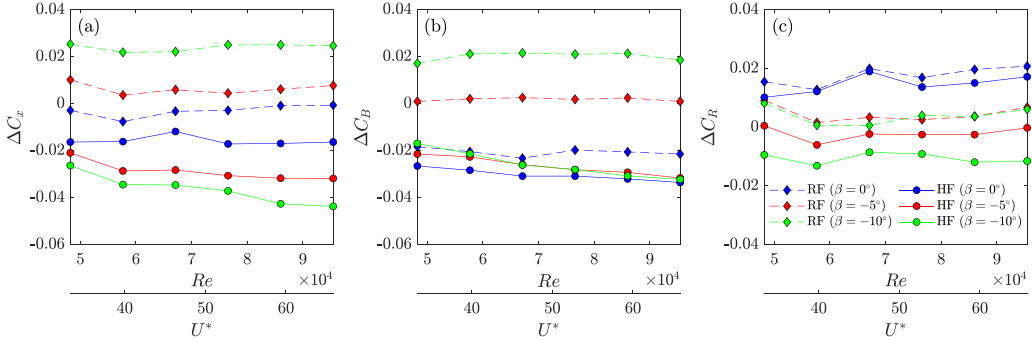
FIG. 4. Evolution of (a) averaged drag, (b) base drag, and (c) remaining drag coefficients relative change with respect to case B ($\Delta C_x$, $\Delta C_B$, and $\Delta C_R$, respectively) against Reynolds number for RF (rigid flaps, diamonds) and HF (hinged flaps, circles) cases at different yaw angles ($\beta = 0°$ in blue, $\beta = -5°$ in red, and $\beta = -10°$ in green).

contribution [see Fig. 4(c)]. Nevertheless, a significant drag reduction is obtained ($\Delta C_x \simeq -4.1\%$) which is approximately constant over the tested range of Re or reduced velocity $U^*$ (see Fig. 4). This improvement attained with respect to the rigid (RF) configuration may be presumably caused by the reconfiguration of flaps occurring when a degree of freedom is introduced with the flexible foil.

Under yawed conditions, the RF configuration is neither capable to reduce $C_x$ nor $C_B$ with respect to the baseline Ahmed body. Their increase, especially at $10°$, must be related to the strong separations at the top and bottom edges of the flaps. In terms of the rest of the body, yaw angle seems to have very little influence on $\Delta C_R$ for the RF configuration.

On the other hand, the hinged flaps (HF) feature increasing reductions of base drag and drag with growing values of $U^*$ (larger relative flexibility) for both $\beta = -5°$ and $-10°$, which may be conveniently used in practical applications to reduce drag under crosswind conditions. In particular, very similar values of $\Delta C_B$ are obtained for both yaw angle values when the HF configuration is set (the obtained changes with respect to base configuration can be seen in Table I). However, the relative drag coefficient reduction, which is larger than that of the base drag $C_B$, increases with the growing value of $\beta$ [see Fig. 4(b)], reaching maximum relative improvements of $\Delta C_x \simeq -7.5\%$ at $\beta = 5°$ and $\Delta C_x \simeq -9.1\%$ at $\beta = 10°$ (see Table I). These results suggest that there is a progressive reconfiguration of the flexible flaps with $U^*$ and $\beta$, which contributes to reduce drag. In this regard,

TABLE I. Drag, base drag, and remaining drag coefficient values in each configuration (Base: B; Rigid flaps: RF; Hinged flaps: HF) for the tested yaw angles at Re $\sim 10^5$. Relative drag $\Delta C_x(\%)$, base drag $\Delta C_B(\%)$, and remaining drag $\Delta C_R(\%)$ changes with respect to B configuration are included.

| Config. | $\beta$(deg) | $C_x$ | $\Delta C_x(\%)$ | $C_B$ | $\Delta C_B(\%)$ | $C_R$ | $\Delta C_R(\%)$ |
|---|---|---|---|---|---|---|---|
| | 0 | 0.380 | – | 0.176 | – | 0.204 | – |
| B | −5 | 0.429 | – | 0.229 | – | 0.200 | – |
| | −10 | 0.482 | – | 0.286 | – | 0.196 | – |
| | 0 | 0.379 | −0.3 | 0.155 | −11.9 | 0.224 | 9.8 |
| RF | −5 | 0.436 | 1.6 | 0.230 | 0.4 | 0.206 | 3.0 |
| | −10 | 0.507 | 5.2 | 0.305 | 6.6 | 0.202 | 3.1 |
| | 0 | 0.364 | −4.2 | 0.143 | −18.8 | 0.221 | 8.3 |
| HF | −5 | 0.397 | −7.5 | 0.197 | −14.0 | 0.200 | 0.0 |
| | −10 | 0.438 | −9.1 | 0.254 | −11.2 | 0.184 | −6.1 |
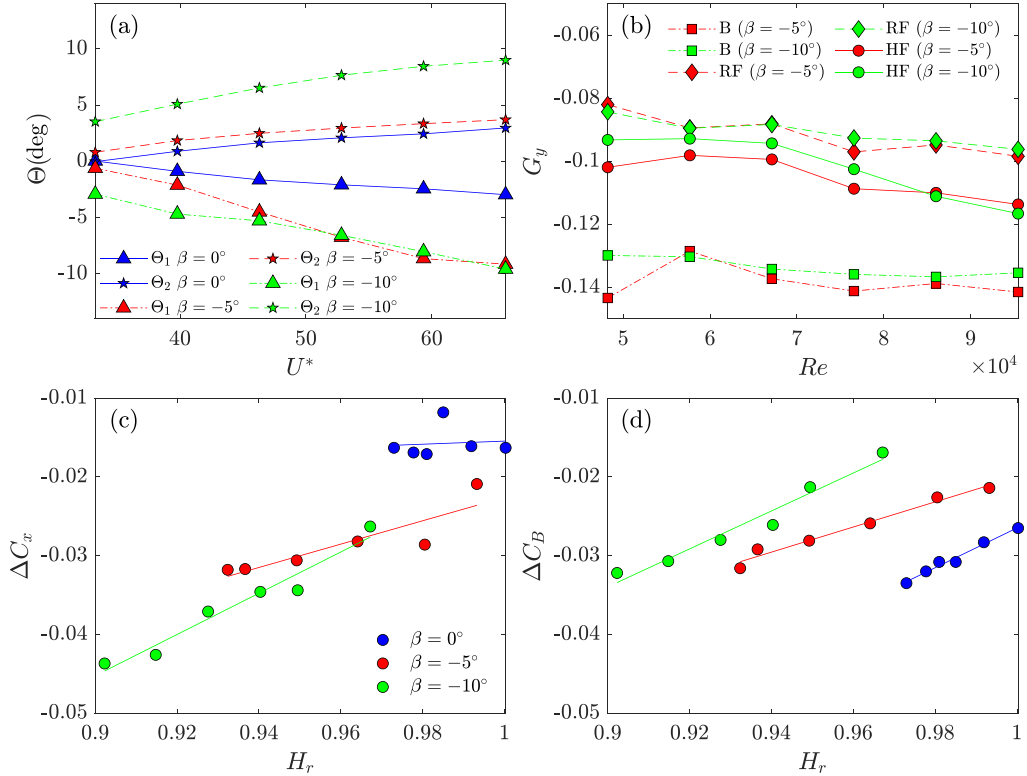
FIG. 5. (a) Evolution of the time-averaged flaps deflection at yaw $\beta = 0°, -5°, -10°$, $\Theta_1$ (leeward flap) and $\Theta_2$ (windward flap) with the reduced velocity $U^*$. (b) Evolution of the time-averaged horizontal pressure gradient $G_y$ with the Reynolds number $Re$ for the three configurations and $\beta = -5°$ and $-10°$. (c), (d) Corresponding correlation of the trailing bluffness $H_r$ with the relative variations of drag (c) and base drag (d) coefficients, $\Delta C_x$ and $\Delta C_B$, with respect to reference values of B configuration, as a function of the yaw angle. Solid lines depicting the associated linear fit are included.

HF is able to produce negative values of $C_R$ [see Fig. 4(c)], so, hinged flaps may produce some thrust on the body, which increases with yaw.

In fact, the hinged flaps may also weaken the strength of vortices originated around the body, which are known to increase the drag [34,36], thus reducing their impact on $C_x$ and providing the additional drag reduction observed here when compared with the trend of $\Delta C_B$. Nevertheless, one can conjecture that the relative contribution of these longitudinal vortices to the drag force increases with $\beta$, and the stronger reconfiguration at large Re or $U^*$ may lead to higher potential for aerodynamic improvement. This is in line with our results, since the slope of $\Delta C_x$ vs $U^*$ is greater than that observed for $\Delta C_B$ at yawed conditions. Besides, as highlighted in previous study by Urquhart *et al.* [22], where optimized asymmetric configurations of flaps are used to reduce drag under yawed conditions, it is likely that the unequal adaption of windward and leeward flaps reduces the cross flow within the near wake, which would contribute to decrease drag. That said, in order to better understand the role of reconfiguration, we next discuss the relationship between $C_B$, $C_x$, $\Theta_1$, and $\Theta_2$.

Figure 5 displays the evolution of time-averaged flap deflections $\Theta_1$ and $\Theta_2$, with respect to the reduced velocity (note that for the sake of conciseness, amplitude of angular fluctuations $\hat{\Theta}_i$, where $i = 1, 2$ are not depicted, as its value lies always below the 15% of the average displacement $\Theta_i$ within the range of $U^*$ and $\beta$ investigated here, and therefore, reconfiguration can be considered

quasistatic at first order). In the following, an outward deflection is used when the flap is oriented towards the exterior of the base, and an inward deflection when oriented towards the interior of the base. That said, initially the flaps are slightly oriented outwards ($\Theta_1 \approx 1°$, $\Theta_2 \approx -1°$) in our experiment due to small precharges in the setup. Nonetheless, the fluid load is able to gradually move them inwards without remarkable influence of the initial position. For aligned flow conditions, $\beta = 0$ in Fig. 5(a), the flaps reconfigure inwards ($\Theta_1 < 0$, $\Theta_2 > 0$), depicting a linear trend. Both flaps deflect inwards nearly symmetrically with a maximum reconfiguration angle of approximately $3°$ at the highest $U^*$ with differences below $0.5°$ for any $U^*$ value. The reconfiguration of the flaps remains below the typical flow separation angles (above $12°$), then, the flow massive separation occurs presumably at their trailing edge.

At yawed conditions, the flaps may deflect asymmetrically as they face differently the incoming wind. At $\beta = -5°$ in Fig. 5(a), the windward flap, $\Theta_2$ deflects with a positive angle [red star symbols in Fig. 5(a)] that tends to compensate the yaw angle and to align with the flow direction. The inwards deflection of the leeward flap $\Theta_1$ shown with red triangle symbols is larger, especially at high $U^*$ implying a significant elastic torque at the hinge balanced by an important pressure difference between both flap sides.

This result seems to be connected to the structure of the recirculation regions for a yawed Ahmed described in Ref. [14]. At the windward side, the flow is parallel to the lateral sides while a large recirculating region is fixed on the leeward side. Then, the pressure gradient between both sides of the flaps is greater at the leeward than at the windward side.

At the higher value of yaw, $\beta = -10°$, the windward flap $\Theta_2$ shown with green star symbols in Fig. 5(a) deflects inwards with $U^*$ reaching values close to the yaw angle indicating a quasialignment with the incoming flow. The leeward flap $\Theta_1$ (green triangle symbols) deflects progressively inwards reaching also the limit of $10°$, a value similar to that observed for the leeward flap at yaw $\beta = -5°$. This observation suggests that the transverse pressure gradient, probably induced by the near-wake asymmetry developed by the increasing yaw, is approximately maintained between $\beta = -5°$ and $-10°$. To check this point, we present in Fig. 5(b) the time-averaged horizontal base pressure gradient $G_y$ as a function of Re, for the three configurations, and yaw angles of $\beta = -5°$ and $-10°$. This magnitude can be used as a quantitative estimate of the near-wake asymmetry. It is observed that, regardless of the configuration considered, B, RF, or HF, the values of $G_y$ for both yawed conditions nearly coincides, which may explain that the leeward flap reconfiguration is similar for both values of the yaw angle shown with red and green triangle symbols in Fig. 5(a) as discussed above. It is also shown that the magnitude of $G_y$ decreases for the controlled configurations RF and HF, when compared to the baseline case, suggesting a weaker wake asymmetry. Interestingly, at high $U^*$, the magnitude of the gradient increases for HF, presumably due to the presence of a RSB mode (that will be confirmed in the following), which is known to amplify the wake asymmetry at yaw compared to a wake with no RSB modes as that obtained with a cavity [14,37].

The asymmetry of the recirculating bubble induced by the yaw also acts on the unsteady flap response. Although the flaps reconfiguration is mostly quasistatic at first order for the range of $U^*$ studied here, we can observe some differences between windward and leeward flaps oscillations, $\hat{\Theta}_i$. While the amplitude of the leeward oscillations remain constant with $U^*$ (around $\hat{\Theta}_1 \sim 0.5$), that of the windward flap vibration increases with $U^*$ (largest values of $\hat{\Theta}_2 \simeq 3$), what may be guided by a stronger shear, as inferred in previous visualizations [14].

The pressure loading on the flaps may also explain the obtained values of $\Delta C_R$, in that sense, one can estimate the thrust produced by the flaps deflection with the torsional stiffness of the joint and the forcing location acting on the flap. Our results, not shown here, indicate a direct relation between that thrust and $\Delta C_R$. Thus, increasing yaw provokes greater flaps' deflection, generating more thrust and therefore, reducing further $C_B$ and $C_x$.

The reconfiguration of the flaps is effective to reduce the drag and the base drag at yawed conditions, as Figs. 5(c), 5(d) show. There, $\Delta C_x$ and $\Delta C_B$ are represented against trailing bluffness, $H_r$, computed from flaps deflection (see Fig. 1). In this regard, the base pressure recovery shows an
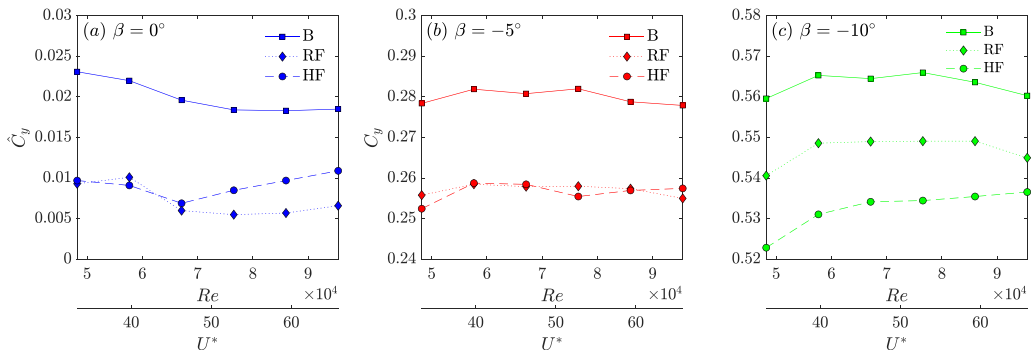
FIG. 6. Evolution of lateral force coefficient with $Re$ at different yaw angles: (a) $\beta = 0°$, (b) $\beta = -5°$, and (c) $\beta = -10°$ for the tested configurations (B, RF, HF). In the case of aligned conditions, $\hat{C}_y$ instead of $C_y$ is depicted.

excellent direct correlation with $H_r$, with a nearly constant slope for the orientations tested in our experiments. In terms of drag, the near-wake bluffness, $H_r$, correlates linearly with $\Delta C_x$ under yaw, although the slope increases with $\beta$. Thus, the flaps reconfiguration seems to be able to increase the base pressure and reduce the drag of the remaining parts of the body (mainly associated with the formation of three-dimensional streamwise vortices on the body edges), thus reducing efficiently the baseline body drag coefficient at yawed conditions. Also, as the yaw increases, their impact on the aerodynamic drag is seen to increase (see Figs. 4, 5).

## B. Lateral forces

Our experimental facility allows us to obtain the lateral forces acting on the model too. At $\beta = 0°$, reflectional-symmetry-breaking (RSB) modes act on our baseline Ahmed body producing the appearance of two equally probable horizontal asymmetric states that produce a significant lateral force [31]. To describe the amplitude of these modes in terms of lateral forces, one has to compute the averaged level of fluctuations of $c_y$ signal, $\hat{C}_y$, since the averaged $C_y$ will just dictate the probability of exploring one of the two asymmetric states [37]. Figure 6(a) shows the evolution of $\hat{C}_y$ with the Reynolds number for the different rear configurations tested here. Case B depicts a lateral force, associated with RSB modes, with an amplitude around 0.02, which agrees with previously reported results.

When rigid lateral flaps (RF) are set, the lateral force amplitude is strongly decreased, suggesting a strong attenuation of RSB modes, as it happens with rigid rear full cavities [10]. More interestingly, hinged flaps behave as rigid flaps at low Reynolds (low values of $U^*$) but $\hat{C}_y$ amplitude grows as the free-stream velocity increases above an intermediate value of $U^*$, which will be shown to be related to the fluid-structure interaction mechanism between the flaps and the RSB modes.

In general, as $U^*$ increases from there, the aerodynamic loading acting on the hinged flaps also increases (as inferred from the inwards flaps displacement shown in Fig. 5) above the value provided by the rigid static flaps. However, the lateral force $\hat{C}_y$ associated with such region of $U^*$ for the HF arrangement remains smaller than that experienced by the baseline Ahmed body, probably because the associated horizontal pressure gradient amplitude is smaller.

Once yaw conditions are set, the value of the time-averaged side force coefficient $C_y$ is naturally affected, and becomes non-nil, as the configuration loses its symmetry [see Figs. 6(b), 6(c)]. As shown in Refs. [37,38], the value of $C_y$ for the baseline Ahmed body varies linearly with $\beta$ (for $|\beta| > 1$). This result is also obtained from the present data, since the coefficient takes the values $C_y \simeq [0, 0.28, 0.56]$ at $\beta = 0°, -5°, -10°$, respectively, for the case B. Adding the flaps (for RF and HF configurations) should increase the lateral force due to the increased length of the body,
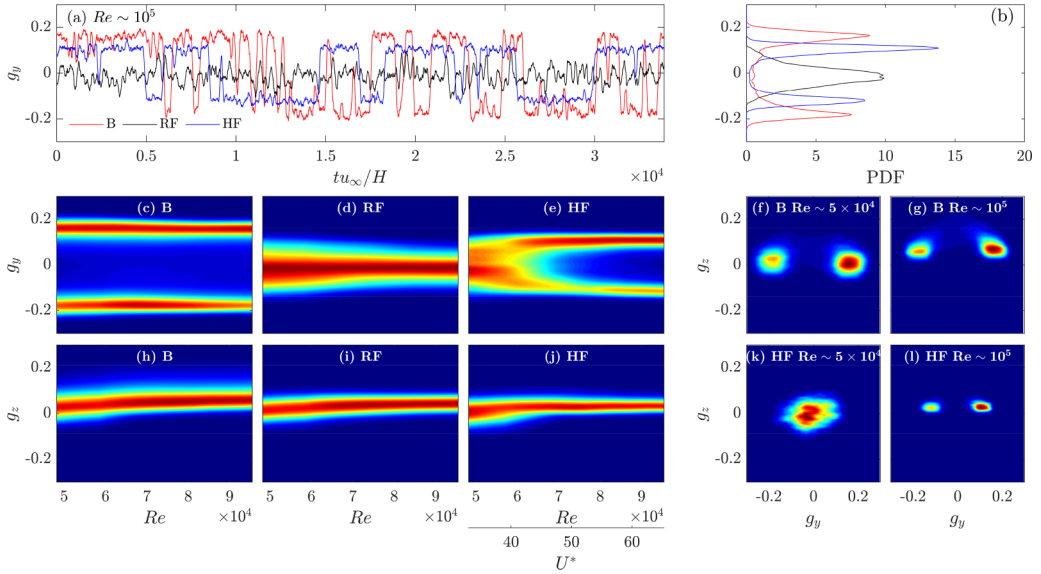
FIG. 7. (a) Temporal evolution of horizontal base pressure gradient, $g_y$, for the tested configurations (B, RF, HF) at $Re \simeq 10^5$. (b) Corresponding probability density (PDF) of $g_y$. Contours of pressure gradients PDFs from (c)–(e) $g_y$ and (h)–(j) $g_z$ at the tested Reynolds number Re (and $U^*$), for the three configurations B, RF, and HF. Joint horizontal and vertical base pressure gradients PDF for selected values of $Re$ for the (f), (g) B and the (k), (l) HF configurations. All PDFs are normalized with their corresponding maxima.

however, this effect is balanced by the reduction of the horizontal base pressure gradient, $G_y$, for both RF and HF in comparison with B configuration [see Fig. 5(b)]. As for $G_y$, the measured side force coefficients do not change significantly with Re at $\beta = -5°$, remaining nearly constant, providing a similar reduction of $C_y$ with rigid and hinged flaps (around 8.3%).

For $\beta = 10°$, cases B and RF show similar trends with Re, indicating that they exhibit an equivalent behavior. Conversely, for the HF case, $C_y$ depicts an increase with Re, suggesting that the aforementioned thrust induced by the torsional joint is also acting on the side force. Moreover, the strong deflection of the flaps at yawed conditions (specially at 10°) may reduce the lateral projected area in comparison with RF configuration, which partially explains the differences depicted in Fig. 6(c). The use of hinged flaps decreases the side loading, when compared to the other two configurations, as $\beta$ grows, showing a general better aerodynamic performance of this system.

## C. Bistable dynamics

In the present section, we will discuss the effect of the rear flaps on the bistable dynamics of the near wake with help of the base pressure measurements. Under symmetric conditions, our experiment presents RSB modes horizontal bistability, so, only $\beta = 0°$ orientation is considered herein.

Figure 7(a) displays the time evolution of the horizontal base pressure gradient, $g_y$, for the tested configurations (B, RF, and HF) at $Re \simeq 10^5$, with the corresponding probability density functions (PDFs) shown in Fig. 7(b). As observed therein, the wake behind the reference case B exhibits, with almost the same probability, two RSB modes characterized by respective positive (P) and negative (N) values of $g_y$ and associated with the two horizontally deflected mirrored wake states reported in Ref. [7]. This bistable dynamics is characterized by an intermittent random switching between negative and positive states of $g_y$. In the vertical direction, the wake is fixed in a position slightly affected by the ground presence, as depicted in Fig. 8(a) at $Re \simeq 10^5$. In order to depict
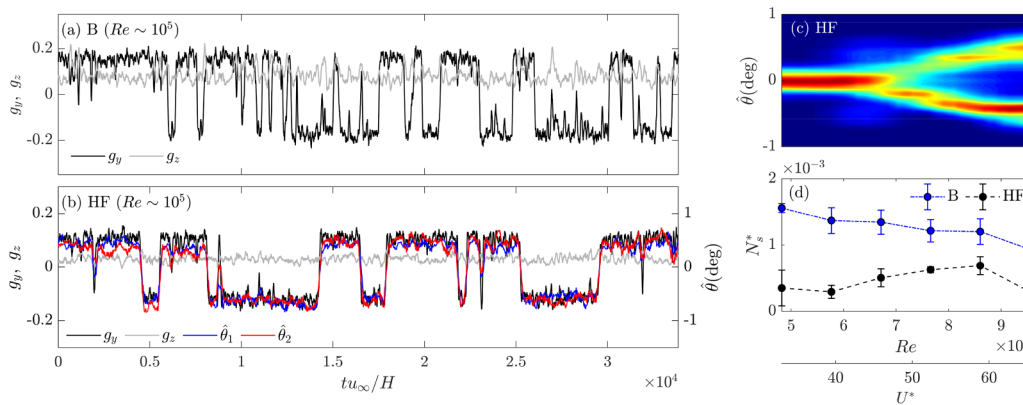
FIG. 8. RSB dynamics at $\beta = 0°$. (a), (b) Temporal evolution of horizontal, vertical base pressure gradients and flap deflection fluctuating angles, $\hat{\theta}_1$ and $\hat{\theta}_2$, for B and HF configurations at Re $\sim 10^5$. (c) PDF of the observed averaged deflected angle, $\hat{\theta}_1$ and $\hat{\theta}_2$, position for HF configuration. The PDF is normalized with its maximum value. (d) Nondimensional switching events, $N_s^*$, evolution with $Re$ for B and HF configurations. Error bars are included for the different tests performed.

a global picture, contours of the horizontal and vertical base pressure gradients PDF are shown in Figs. 7(c)–7(e), 7(h)–7(j) at the tested Re for the three configurations employed here (B, RF, HF).

For the B case, symmetrical bistable dynamics are preserved at any tested Re condition [Fig. 7(c)]. Additionally, the vertical base pressure gradient $g_z$ [Fig. 7(h)], remains positive along the whole range of Re, showing a slight increase in its value with Re, on account of the ground effect, which decreases pressure at the bottom of the base. The bistable dynamics in the horizontal axis $y$ and the slight increase of the wake asymmetry in the vertical axis $z$ is also illustrated with help of the joint PDF in Figs. 7(f), 7(g).

When the rigid flaps are installed, the wake is symmetrized and the RSB modes are stabilized. This can be observed in the PDF of $g_y$ [Figs. 7(b), 7(d)], which now features a single peak with no trace of the bistable switching dynamics [see Fig. 7(a)]. The lateral rigid flaps move the separation point far from the body base and reduce the separated mixing layers interaction, which eliminates the RSB modes [9]. Their effect on the vertical asymmetry is weak, showing a slight sharpening of the peak [Fig. 7(i)].

Interestingly, the use of hinged flaps produces a hybrid wake behavior between both previous dynamics. In particular, as depicted in Fig. 7(e), when the reduced velocity $U^*$ (or Re) is small, the PDF of the horizontal gradient $g_y$ covers a wider region of values, suggesting that the RSB modes explore different locations around a central plane. This means that the wake undergoes a sort of weak symmetrization and does not display a complete stabilization of the RSB modes, on account of the finite stiffness value of the flaps $U^* > 0$. Note that the rigid flaps correspond to the particular case $U^* \to 0$.

However, around $U^* \simeq 45$ the wake displays a transition towards a bistable behavior, and $g_y$ starts to explore again positive and negative $g_y$ values associated with P and N states of the RSB modes in the horizontal direction [see Figs. 7(a), 7(b)] (the destabilization of the RSB modes confirms the previous observation of the amplification of the base pressure gradient at yaw with hinged flaps at higher Re). The qualitative change between both regimes is clearly illustrated in the joint PDF [Figs. 7(k), 7(l)]. Interestingly, the flaps displacement is sensitive to such changes in the pressure gradient, and they fluctuate around a mean-shifted location, following the switches of $g_y$, as shown in the time series and the corresponding PDF of deflection fluctuating amplitude $\hat{\theta}$ depicted in Figs. 8(b), 8(c). There, two equiprobable branches of dynamic response can be observed for $\hat{\theta}$ corresponding to P and N states.
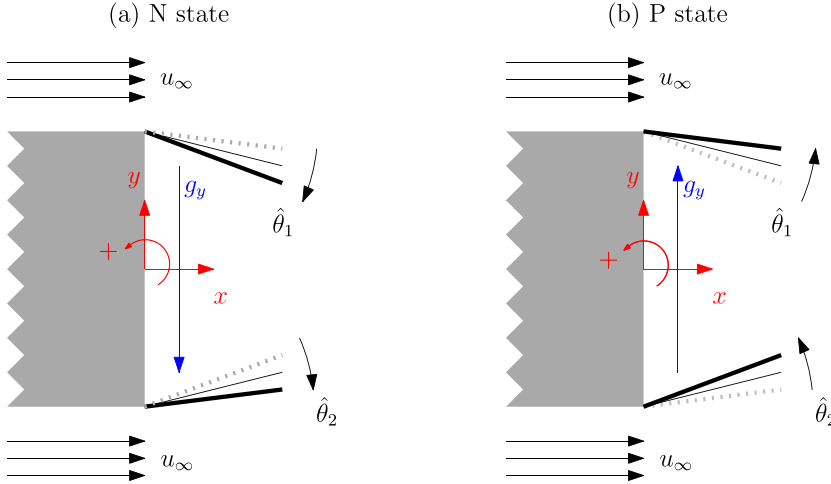
FIG. 9. Sketch of the interaction between flaps and the RSB mode: (a) N state observed with negative flaps deflection and (b) P state observed with positive flaps deflection. Flaps are represented using thick solid lines, while thin solid lines indicates mean deflected positions. Dashed lines are the flaps deflection of the opposite state that is not observed.

Notwithstanding, the bistable dynamics is qualitatively different from that of the baseline case. As depicted in Figs. 8(a), 8(b) the use of hinged flaps slows down the switching dynamics, as the time evolution of $g_y$ displays fewer switches between P and N states compared to the baseline case. This effect is presumably a consequence of the feedback of the flaps deflection on the RSB modes. Actually it has been shown in Refs. [18,19] that small positive (negative) flaps deflection selects preferentially a RSB mode in a P (N) $g_y$ state. Actually, Fig. 8(b) shows that the flaps deflection and the horizontal pressure gradient are synchronized with identical signs. Moreover, it is likely that the configuration flaps deflection/$g_y$ state corresponds to an equilibrium of the elastic flaps, where the more deflected flap is maintained by the low-pressure side of the RSB mode $g_y$ gradient and the less deflected flap is maintained by the high pressure of the gradient. This is illustrated in Fig. 9, where asymmetric deflections of flaps are sketched for the positive (P state) and negative (N state) base pressure gradient $g_y$ involved in the fluid-structure interaction dynamics of Fig. 8(b).

The increase of the state probability due to the flap orientation might explain the decrease of switching events. Further investigations of this mechanism with the present experiment are, however, limited by the lack of synchronization of both the acquisition of the pressure gradient and the flaps deflection. A fluid structure interaction with the RSB mode has previously been reported by Ref. [39] in the case of free-rotating rectangular plates facing a uniform flow. In such a configuration, the rectangular plate deflection selects the RSB mode that creates the plate disequilibrium thus conducting to a stochastic dynamic of the deflection angle [see Figs. 7(a), 8(b)].

It can also be seen in Figs. 7(a), 8(b) that the amplitude of $g_y$ decreases when the flexible flaps are used compared to the baseline case (i.e., $|g_y|_{HF} \simeq 0.11$ vs. $|g_y|_B \simeq 0.19$). This demonstrates that the hinged flaps manage to attenuate the wake asymmetry even if the wake dynamics is still bistable, which leads to a smaller fluctuating amplitude of the side force $\hat{C}_y$, as discussed in Fig. 6.

The slowing down of the bistable dynamics between both configurations is further illustrated in Fig. 8(d), which shows the nondimensional number of switches between positive (P) and negative (N) values of $g_y$, $N_s^*$ (computed as $N_s h/t u_\infty$), versus $U^*$. Specifically, the number of switches has been computed by using a threshold of $|g_y| \geqslant 0.09$ to define the RSB asymmetric state. Note that, as there are different horizontal pressure gradient amplitudes for asymmetric states in the two different configurations, a common robust threshold has been selected by means of statistic postprocessing, thus allowing to quantitatively characterize and compare the bistable dynamics.

As expected, few switches are identified below the critical value of $U_{cr}^* \simeq 45$, whereas $N^*$ increases progressively from there on, with the reduced velocity, as the relative stiffness of hinges decreases and the coupled fluid-structure dynamics speeds up [note that $N^*$ is not zero below $U_{cr}^*$ since the value of $g_y$ explores a wide range of values as the center of pressure meanders on the base, as illustrated in Fig. 7(e)]. For the whole range of reduced velocity investigated, the number of switches for the baseline case remains above that of the hinged system, confirming the slower switching dynamics of the bistability as the flexible flaps are used.

Finally, as an additional comment, one may expect that, in view of these results, lighter flaps featuring lower mass-damping parameter $\zeta m^*$ induce a stronger dynamic response, thus leading to bistable dynamics, even at low values of $U^*$, which could be detrimental from the control point of view.

## IV. CONCLUSIONS

The performance of hinged lateral flaps (HF) as drag reducers has been tested in a square-back Ahmed body subject to turbulent flow with Re $\in [0.5, 1] \times 10^5$ under different yaw conditions. Their effects have been compared with baseline body (B) and equivalent lateral rigid flaps (RF) arrangement by means of force, pressure, and deflection measurements in wind tunnel tests. For the range of parameters used herein, it has been found that the hinged flaps deflection is almost quasistatic at first order when the different flow conditions are set. They display a clear example of passive reconfiguration, which has been shown to be the key element to produce important modifications in the interaction between the turbulent flow field and the different rear ends. While the rigid flaps do not produce significant drag changes, even if they increase the base pressure, due to their additional length, the use of hinged flaps manages to efficiently reduce both base drag and drag coefficients for aligned and yawed conditions. In this regard, the mechanism of drag reduction is based on base pressure recovery, topology changes of streamwise vortices at the body edges and the effect of the flap deflection. Besides, their enhanced performance increases with Re and yaw angle, within the range studied herein. Thus, comparing the present system with previously developed control devices using optimized asymmetric flaps (see, e.g., Refs. [19,22]), it can be concluded that appropriate design of self-adaptive flexible flaps (i.e., selection of $U^*$ and $m^*\xi$ parameters) provides similar drag reductions, above 9% under maximum yaw angle. In addition, the passive adaption undergone by the flexible flaps defines quasistatic, inwards deflections, even for the windward side, differently from what was obtained in Ref. [22], although such option was identified therein as a further improvement of the optimization process to reduce cross flow inside the near wake.

Moreover, the employed configurations (B, RF, and HF) interact differently with RSB modes at aligned conditions. The wake behind the baseline body depicts the classical bistable behavior described in the literature. The rigid flaps are able to symmetrize the wake in the horizontal direction as closed cavities do. However, the hinged flaps configuration features two different dynamics behaviors as $U^*$ increases. Thus, below a critical value of the reduced velocity $U^* < U_{cr}^*$, the hinged flaps behave as rigid flaps, inducing symmetrization at the wake, without a clear trace of asymmetric deflected states (P or N) related to RSB modes. On the other hand, for $U^* > U_{cr}^*$, the hinged flaps deflect following changes in the horizontal pressure gradient given by the switches between RSB modes, thus describing a bistable behavior, with a decrease of the switching rate revealing a fluid structure interaction mechanism. The interaction of the RSB mode and the elastic flap deflection offers perspectives on the fundamental background requiring further experimental investigation that we wish to compare with the stochastic model developed by Ref. [40].

For nonaligned wind conditions, the combined advantages in terms of drag and side forces suggests an interesting potential for the use of hinged flaps in real applications with heavy vehicles, where passive reconfiguration may help improving the global aerodynamic and the adaptability of control systems to changing flow conditions (note that similar properties of rear separation may be expected for higher Reynolds numbers in the Ahmed body, although present results may be considered carefully, and the comparison in terms of drag and pressure coefficients may change in

real applications). To that aim, higher Reynolds number tests with more realistic geometries, precise design of the system, and selection of fluid-structure interaction parameters, e.g., reduced velocity and mass-damping ratio, may be required to properly adapt the present solution to heavy vehicles applications.

[1] S. R. Ahmed, G. Ramm, and G. Faltin, Some salient features of the time-averaged ground vehicle wake, SAE Trans. **93**, 473 (1984).

[2] W. Hucho and G. Sovran, Aerodynamics of road vehicles, Annu. Rev. Fluid Mech. **25**, 485 (1993).

[3] R. M. Wood and S. X. Bauer, Simple and low-cost aerodynamic drag reduction devices for tractor-trailer trucks, SAE Tech. Pap. **112**, 143 (2003).

[4] H. Choi, J. Lee, and H. Park, Aerodynamics of heavy vehicles, Annu. Rev. Fluid Mech. **46**, 441 (2014).

[5] E. G. Duell and A. R. George, Experimental study of a ground vehicle body unsteady near wake, SAE Trans. **108**, 1589 (1999).

[6] B. Khalighi, S. Zhang, C. Koromilas, S. Balkanyi, L. P. Bernal, G. Iaccarino, and P. Moin, Experimental and computational study of unsteady wake flow behind a bluff body with a drag reduction device, SAE Trans. **110**, 1209 (2001).

[7] M. Grandemange, M. Gohlke, and O. Cadot, Turbulent wake past a three-dimensional blunt body. Part 1: Global modes and bi-stability, J. Fluid Mech. **722**, 51 (2013).

[8] M. Grandemange, M. Gohlke, and O. Cadot, Turbulent wake past a three-dimensional blunt body. Part 2: Experimental sensitivity analysis, J. Fluid Mech. **752**, 439 (2014).

[9] Y. Haffner, J. Borée, A. Spohn, and T. Castelain, Mechanics of bluff body drag reduction during transient near-wake reversals, J. Fluid Mech. **894**, A14 (2020).

[10] A. Evrard, O. Cadot, V. Herbert, D. Ricot, R. Vigneron, and J. Délery, Fluid force and symmetry breaking modes of a 3D bluff body with a base cavity, J. Fluids Struct. **61**, 99 (2016).

[11] A. D'Hooge, R. Palin, L. Rebbeck, J. Gargoloff, and B. Duncan, Alternative simulation methods for assessing aerodynamic drag in realistic crosswind, SAE Int. J. Passeng. Cars - Mech. Syst. **7**, 617 (2014).

[12] J. Howell, M. Passmore, and S. Windsor, A drag coefficient for test cycle application, SAE Int. J. Passeng. Cars - Mech. Syst. **11**, 447 (2018).

[13] Y. Fan, V. Parezanović, and O. Cadot, Wake transitions and steady-instability of an ahmed body in varying flow conditions, J. Fluid Mech. **942**, A22 (2022).

[14] M. Lorite-Díez, J. I. Jiménez-González, L. Pastur, O. Cadot, and C. Martínez-Bazán, Drag reduction on a three-dimensional blunt body with different rear cavities under cross-wind conditions, J. Wind Eng. Ind. Aerod. **200**, 104145 (2020).

[15] M. Lorite-Díez, J. Jiménez-González, C. Gutiérrez-Montes, and C. Martínez-Bazán, Drag reduction of slender blunt-based bodies using optimized rear cavities, J. Fluids Struct. **74**, 158 (2017).

[16] M. Hassaan, D. Badlani, and M. Nazarinia, On the effect of boat-tails on a simplified heavy vehicle geometry under crosswinds, J. Wind Eng. Ind. Aerod. **183**, 172 (2018).

[17] R. Li, J. Borée, B. R. Noack, L. Cordier, and F. Harambat, Drag reduction mechanisms of a car model at moderate yaw by bi-frequency forcing, Phys. Rev. Fluids **4**, 034604 (2019).

[18] R. D. Brackston, J. M. García de la Cruz, A. Wynn, G. Rigas, and J. F. Morrison, Stochastic modelling and feedback control of bistability in a turbulent bluff body wake, J. Fluid Mech. **802**, 726 (2016).

[19] J. M. García de la Cruz, R. D. Brackston, and J. F. Morrison, Adaptive base-flaps under variable cross-wind, Technical Paper 2017-01-7000, SAE International, 2017.

[20] M. Varney, M. Passmore, and A. Gaylard, Parametric study of asymmetric side tapering in constant cross wind conditions, in *WCX World Congress Experience* (SAE International, Warrendale, 2018).

[21] M. Urquhart, M. Varney, S. Sebben, and M. Passmore, Drag reduction mechanisms on a generic square-back vehicle using an optimised yaw-insensitive base cavity, Exp. Fluids **62**, 241 (2021).

[22] M. Urquhart, M. Varney, S. Sebben, and M. Passmore, Aerodynamic drag improvements on a square-back vehicle at yaw using a tapered cavity and asymmetric flaps, Int. J. Heat Fluid Flow **86**, 108737 (2020).

[23] M. Urquhart, and S. Sebben, Optimisation of trailing edge flaps on the base cavity of a vehicle for improved performance at yaw, Flow, Turbul. Combust. **109**, 309 (2022).

[24] E. de Langre, Effects of wind on plants, Annu. Rev. Fluid Mech. **40**, 141 (2008).

[25] F. Gosselin, E. de Langre, and B. A. Machado-Almeida, Drag reduction of flexible plates by reconfiguration, J. Fluid Mech. **650**, 319 (2010).

[26] N. Mazellier, A. Feuvrier, and A. Kourta, Biomimetic bluff body drag reduction by self-adaptive porous flaps, Comp. Rend. Méc. **340**, 81 (2012).

[27] C. García-Baena, J. I. Jiménez-González, and C. Martínez-Bazán, Drag reduction of a blunt body through reconfiguration of rear flexible plates, Phys. Fluids **33**, 045102 (2021).

[28] C. García-Baena, J. I. Jiménez-González, C. Gutiérrez-Montes, and C. Martínez-Bazán, Numerical analysis of the flow induced vibrations in the laminar wake behind a blunt body with rear flexible cavities, J. Fluids Struct. **100**, 103194 (2021).

[29] J. Jiménez-González, C. Garcí-Baena, J. Aceituno, and C. Martínez-Bazán, Flow-induced vibrations of a hinged cavity at the rear of a blunt-based body subject to laminar flow, J. Sound Vib. **495**, 115899 (2021).

[30] C. García-Baena, J. Camacho-Sánchez, M. Lorite-Díez, J. I. Jiménez-González, and C. Gutiérrez-Montes, Drag improvement on a blunt-base body by self-adaption of rear flexibly hinged flaps, J. Fluids Struct. **118** 103854 (2023).

[31] M. Grandemange, M. Gohlke, and O. Cadot, Bi-stability in the turbulent wake past parallelepiped bodies with various aspect ratios and wall effects, Phys. Fluids **25**, 095103 (2013).

[32] A. Roshko, Perspectives on bluff body aerodynamics, J. Wind Eng. Ind. Aerod. **49**, 79 (1993).

[33] D. Barros, J. Borée, O. Cadot, A. Spohn, and B.R. Noack, Forcing symmetry exchanges and flow reversals in turbulent wakes, J. Fluid Mech. **829 (R1)** (2017).

[34] D. McArthur, D. Burton, M. Thompson, and J. Sheridan, An experimental characterisation of the wake of a detailed heavy vehicle in cross-wind, J. Wind Eng. Ind. Aerod. **175**, 364 (2018).

[35] T. I. Khan, V. Parezanović, L. Pastur, and O. Cadot, Suppression of the wake steady asymmetry of an ahmed body by central base bleed, Phys. Rev. Fluids **7**, 083902 (2022).

[36] S. Satheesh, L. Cordier, F. Kerhervé, and A. Spohn, Yawed ahmed body: impact of vertical flaps on flow structures, in *12th International Symposium on Turbulence and Shear Flow Phenomena (TSFP12)* (2022).

[37] G. Bonnavion and O. Cadot, Unstable wake dynamics of rectangular flat-backed bluff bodies with inclination and ground proximity, J. Fluid Mech. **854**, 196 (2018).

[38] M. Lorite-Díez, J. I. Jiménez-González, L. Pastur, C. Martínez-Bazán, and O. Cadot, Experimental sensitivity analyses of modes to blowing at the base of a 3d bluff body, J. Fluid Mech. **883**, A53 (2020).

[39] O. Cadot, Stochastic fluid structure interaction of three-dimensional plates facing a uniform flow, J. Fluid Mech. **794**, R1 (2016).

[40] E. Boujo and O. Cadot, Stochastic modeling of a freely rotating disk facing a uniform flow, J. Fluids Struct. **86**, 34 (2019).